2D Materials

PAPER

Origin of the complex Raman tensor elements in single-layer triclinic $ReSe_2$

To cite this article: Geovani C Resende *et al* 2021 *2D Mater.* **8** 025002

IOP Publishing 2D Mater. 8 (2021) 025002 https://doi.org/10.1088/2053-1583/abce07

2D Materials

RECEIVED
24 July 2020

REVISED
20 November 2020

ACCEPTED FOR PUBLICATION
25 November 2020

PUBLISHED
17 December 2020

PAPER

Origin of the complex Raman tensor elements in single-layer triclinic $ReSe_2$

Geovani C Resende[1], **Guilherme A S Ribeiro**[1], **Orlando J Silveira**[2], **Jessica S Lemos**[1], **Juliana C Brant**[1], **Daniel Rhodes**[3], **Luis Balicas**[3], **Mauricio Terrones**[4], **Mario S C Mazzoni**[1], **Cristiano Fantini**[1], **Bruno R Carvalho**[5] **and Marcos A Pimenta**[1]

[1] Departamento de Física, Universidade Federal de Minas Gerais, Belo Horizonte Minas Gerais 30123-970, Brazil
[2] Department of Applied Physics, Aalto University School of Science, PO Box 15 100, 00076 Aalto, Finland
[3] National High Magnetic Field Laboratory and Physics Department, Florida State University, Tallahassee, FL 32310, United States of America
[4] Department of Physics, Center for 2-Dimensional and Layered Materials, 2-Dimensional Crystal Consortium, and Department of Chemistry and Department of Materials Science and Engineering, The Pennsylvania State University, University Park, PA 16802, United States of America
[5] Departamento de Física, Universidade Federal do Rio Grande do Norte, Natal Rio Grande do Norte 59078-970, Brazil

E-mail: gcresende@fisica.ufmg.br, brunorc@fisica.ufrn.br **and** mpimenta@fisica.ufmg.br

Keywords: $ReSe_2$, Raman spectroscopy, Raman tensor, electron–phonon coupling, band structure, phonon, transition metal dichalcogenides

Abstract

Low symmetry 2D materials offer an alternative for the fabrication of optoelectronic devices which are sensitive to light polarization. The investigation of electron–phonon interactions in these materials is essential since they affect the electrical conductivity. Raman scattering probes light–matter and electron–phonon interactions, and their anisotropies are described by the Raman tensor. The tensor elements can have complex values, but the origin of this behavior in 2D materials is not yet well established. In this work, we studied a single-layer triclinic $ReSe_2$ by angle-dependent polarized Raman spectroscopy. The obtained values of the Raman tensor elements for each mode can be understood by considering a new coordinate system, which determines the physical origin of the complex nature of the Raman tensor elements. Our results are explained in terms of anisotropy of the electron–phonon coupling relevant to the engineering of new optoelectronic devices based on low-symmetry 2D materials.

1. Introduction

Since the discovery of graphene more than a decade ago [1], other 2D materials were produced and their fundamental properties have been investigated [2, 3]. With the 2D field progressing, it is essential now to study low-symmetry 2D materials which exhibit anisotropy in their properties, such as the electrical [4–6], thermal [7], optical [8] and vibrational [9, 10] ones. Phosphorene [9] crystals and some compounds of the transition metal dichalcogenides family such as 1T′-WTe_2 [11], 1T′-$MoTe_2$ [12], 1T′-ReS_2 [13], and 1T′-$ReSe_2$ [14] crystals, exhibit low symmetries and anisotropic properties. Among these materials, the triclinic rhenium diselenide, $ReSe_2$, exhibits the lowest symmetry and only few reports can be found about its atomic structure [15] and the possible applications as photodetectors and transistors [16–18]. Since different physical properties, such as the electrical and thermal conductivities, are affected by the interactions of electrons and phonons, the study of the anisotropy of the electron–phonon interactions is essential for their application in anisotropic 2D devices, sensitive to the current direction and light polarization [16].

Raman spectroscopy is a fundamental tool to investigate electron–phonon interactions, and their anisotropic behavior in low-symmetry systems, which can be obtained experimentally by controlling the polarization of both the incident and scattered photons with respect to the crystallographic axes. The anisotropy of the Raman response is described by the second-order Raman tensor, whose elements are normally real numbers multiplied by a global phase (ϕ) factor which plays no role in the Raman intensity, and under those circumstances, real numbers are used to describe Raman tensor elements. In fact, the global phase ϕ of the tensor elements cannot be obtained from the Raman measurements of systems with trigonal, tetragonal, hexagonal and cubic symmetries, since it disappears when we take the square modulus of the tensor in order to obtain the Raman intensity. However, when the material absorbs light, these elements can exhibit a relative phase to each other that plays an important role in the Raman intensity [9–12, 19–22]. The complex nature of the Raman tensor elements was reported in previous works in different low-symmetry 2D materials [9–12, 20–22]. For bulk or many layer low-symmetry crystals, another relative phase of the tensor elements can be associated with birefringence, but this effect becomes negligible in a single atomic layer since its thickness is too small when compared to the wavelength of the excitation photon. Kranert *et al* [23] have shown that an observable phase difference between the Raman tensor elements due to birefringence effect becomes appreciable when the thickness of the sample is greater than the wavelength of the incident light.

Single-layer triclinic $ReSe_2$ belongs to the low-symmetry C_i point group, which has only the identity and inversion symmetry elements [24]. All the atoms of its unit cell are displaced from the inversion symmetry center [14, 20]. $ReSe_2$ possesses a large unit cell composed of 12 atoms (4 rhenium and 8 selenium atoms), and exhibits diamond-shaped metal-metal bonds forming a quasi-one-dimensional rhenium chains [24–26]. According to group theory, the Raman spectrum of $ReSe_2$ exhibits 18 non-degenerate first-order modes, all of them belonging to the totally symmetric (A_g) irreducible representation [14, 20]. Due to the low structural symmetry, the intensities of these Raman modes strongly depend on the incident and scattered light polarization [14, 20, 27]. Moreover, they also depend on the direction of the z-axis of the sample, since there is no symmetry operation in $ReSe_2$ that relates z to $-z$ [28]. Choi *et al* reported the observation of 18 A_g modes [22], but a complete analysis of the Raman tensor elements has not yet been performed [14, 16, 22, 27, 29].

In this work, we unravel the fundamental origin of the complex values of the Raman tensor elements in a single-layer of $ReSe_2$. We measured the angle-dependent polarized Raman spectra in both parallel and crossed configurations, and observed that most of the phonons exhibit Raman tensor elements with relative phases. We show that, in order to extract the physical information of the tensor elements, we need to use a new coordinate system of axes, which is specific for each phonon mode. This analysis allowed us to separate all Raman modes in three different classes, according to the phase difference of the Raman tensor elements, considering the excitation laser energy used in this work. First-principles calculations shows that the electron–phonon coupling is more significant at specific points of the Brillouin zone for each phonon mode, evidencing the anisotropy of the electron–phonon interactions. Our result provides a fundamental understanding of the complex Raman tensor elements and highlights the importance of considering the anisotropy of the electron-phonon single-layer $ReSe_2$ in order to explain the experimental results.

2. Results

Initially, we stress the importance of using appropriate experimental procedures in order to obtain the correct values of the Raman tensor elements from the analysis of the angle dependence of the polarized spectra. First, it is fundamental to measure both the parallel (I_{HH}) and cross-polarized (I_{VH}) intensities, in order to perform the correct analysis of the experimental data. Experiments performed without using an analyzer to control the polarization of the scattered light can produce misleading results. Moreover, the sample needs to be placed onto a glass substrate (coverslip) in order to avoid interference effects with the SiO_2/Si substrate, that affect the Raman signal [30–32] preventing the correct analysis of the angular dependence of the polarized Raman spectra.

2.1. Raman-active modes

We start by probing the 18 A_g non-degenerate first-order modes predicted by group theory analysis for this material [14]. Figure 1(a) shows the Raman spectrum in the 100–305 cm^{-1} spectral range of an exfoliated single-layer $ReSe_2$ placed on a silicon substrate covered with a 300 nm thick SiO_2 layer for an excitation energy of 2.34 eV (see Methods). We stress that the Raman spectrum of the sample placed on SiO_2/Si (see figure 1(a)) was only used to calibrate the frequency position of the A_g modes. The Raman spectrum shown in figure 1(a) was collected considering the polarization of both incident and scattered light aligned along the long edge of the sample (see figure S1), which corresponds to the b-axis according to previous reports [22, 33], and it is further confirmed here by using the angular dependence of the Raman spectra (see below). In figure 1(a), the experimental data (blue lozenges) were fitted using a set of Lorentzian functions (orange curves) to track the frequency position, the linewidth, and the relative intensity of each Raman mode. The intensities were arbitrarily increased in the 150–305 cm^{-1} spectral range for better visualization of the peaks.

In figure 1(a), all the 18 A_g Raman modes predicted by group theory are observed in the 100–305 cm^{-1} spectral range with the lowest and highest frequency modes appearing at 107.9 cm^{-1} (A_g^1) and 297.1 cm^{-1} (A_g^{18}), respectively. Here, we assign the 18 A_g modes as A_g^k, where $k = 1$ to 18 in order of increasing frequency. The measured frequencies of our work are in good agreement with the theoretical results [18] (see table S1). It is noteworthy that these 18 modes were not completely probed in references [14, 16, 27, 29], which may be due to the configuration of the experimental setup used to perform the polarized Raman measurements. Recently, Choi *et al* have probed the 18 A_g modes in the $\overline{Z}(HH)Z$ configuration [22]. In our work, the frequency positions of the A_g modes were calibrated relative to the silicon peak located at 521.6 cm^{-1}, and show good agreement with reference [22]. These results highlight the importance of controlling the polarization of both the incident and scattered light when collecting the Raman spectrum in ReSe$_2$-like materials. To further understand this, we next present the angular dependence of the Raman response for each mode.

2.2. Polarized Raman Spectroscopy

The importance of the sample's orientation with respect to the polarization of the incident and scattered lights is crucial when the crystal has low symmetry. Experimentally, we use a half-wave plate to control the horizontal (H) or vertical (V) polarization of the incident light, and an analyzer is used to collect the Raman spectrum in the horizontal polarization. Using this experimental setup, we have performed polarized Raman measurements in the backscattering parallel ($\overline{Z}(HH)Z$) and crossed ($\overline{Z}(VH)Z$) configurations, using a 2.34 eV laser excitation energy (see Methods).

Because ReSe$_2$ has no symmetry under a rotation of π about any in-plane axis, distinct Raman spectra are observed when the sample is either up or down [28]. Furthermore, it is known that an enhancement in the Raman intensity can occur due to multiple reflections of light within the SiO$_2$ layer above the silicon substrate [10, 34]. This effect can infer some systematic errors when the sample is placed on a SiO$_2$/Si substrate (see figure S2). Hence, in order to discard any interference effects from the substrate, we have exfoliated the ReSe$_2$ onto a glass coverslip. From now on, our analyses are based on the data obtained from this sample, which correspond to the *c*-up orientation defined in a previous report [22], obtained by comparing the angular dependence of the Raman response in both works. From the same comparison, we define the *x*-axis as along the long edge of the sample (see figure S1), which is indeed the crystallographic *b*-axis of the sample.

Figures 1(b) and (c) show the angular dependence of the polarized Raman spectra of a single-layer ReSe$_2$ on the coverslip for parallel and cross-configurations in the 100–305 cm^{-1} spectral range for different angles. For both configurations, the spectra were collected under the same experimental conditions: same laser power, exposure time with optimized focus in each measurement, and grating positioning. The spectra were not normalized, i.e. figures 1(b) and (c) have the same scale, where only a smooth baseline was subtracted from the presented spectra.

In figures 1(b) and (c), one observes that most of the Raman modes are more intense in the parallel than in the crossed configuration. For instance, the A_g^4 mode located at 124.9 cm^{-1} is the most pronounced in the parallel configuration, and its intensity remains practically the same for all angles in this configuration (a close-up of this mode in both configurations is shown in figure S3). However, its intensity considerably decreases for some angles in the cross configuration (see figure 1(c)). Additionally, the superimposed modes, A_g^6 (175.7 cm^{-1}), A_g^7 (178.9 cm^{-1}), and A_g^8 (181.9 cm^{-1}) have their intensity weakened in the crossed configuration (see figure 1(c)). The latter mode is more evident in our work than in previous reports [14, 27] due to the spectral resolution of our setup.

Figures 1(d) and (e) show the polarized Raman map obtained for both configurations. The intensity is represented in a logarithmic color scale to better visualize the angular dependence of the low-intensity Raman modes. We can clearly observe a periodicity of 180° in the peak intensity in the parallel configuration in figure 1(d), while the 90° periodicity of the crossed configuration is evident in figure 1(e).

The intensity variation between these configurations is given by the expression [35]:

$$I \propto \left| \hat{e}_i \cdot \overleftrightarrow{R}^k \cdot \hat{e}_s \right|^2, \tag{1}$$

where $\hat{e}_i$ and $\hat{e}_s$ are the polarization vectors of the incident and scattered light, respectively. The $\overleftrightarrow{R}^k$ is the Raman tensor for the *k*-th mode, which can assume complex elements with relative phases when the excitation energy is above the band gap [9, 19, 23]. As it will be shown below, our results are only completely described by considering complex values for the Raman tensor elements in the fitting process.

For a triclinic crystal, the accessible part of the Raman tensor in our backscattering geometry for a A_g mode is given by [20]:

$$\overleftrightarrow{R} = \begin{pmatrix} u e^{i\phi_u} & v e^{i\phi_v} \\ v e^{i\phi_v} & w e^{i\phi_w} \end{pmatrix}, \tag{2}$$

where $u, v, w \geq 0$. Thereby, for a clockwise rotation of the $\hat{e}_i$ and $\hat{e}_s$ vectors, the intensities for the parallel and crossed configurations, and their sum can be written as:

$$\begin{aligned} I_{HH} \propto\; & u^2 \cos^4\theta + w^2 \sin^4\theta + (v \sin 2\theta)^2 \\ & + \sin 2\theta \left(\frac{1}{2} uw \cos\phi_{uw} \sin 2\theta \right. \\ & \left. - 2uv \cos\phi_{uv} \cos^2\theta - 2wv \cos\phi_{wv} \sin^2\theta \right), \end{aligned} \tag{3}$$

$$I_{VH} \propto \left(u^2 + w^2 - 2uw \cos\phi_{uw} \right) \left(\frac{1}{2} \sin 2\theta \right)^2$$

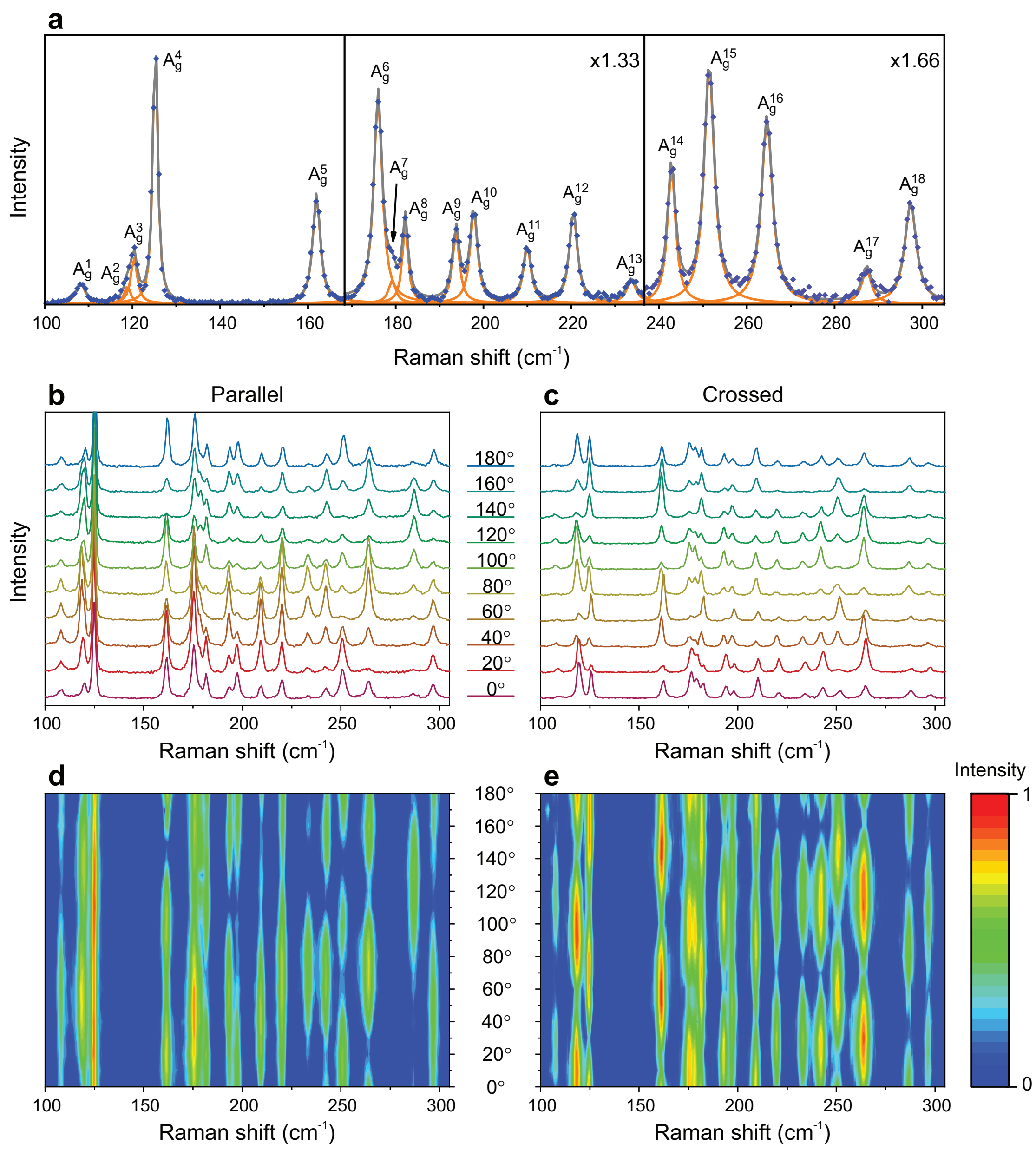

Figure 1. Raman fingerprint of a single-layer ReSe₂. (a) Raman spectrum (blue lozenges) showing the 18 A_g non-degenerate first-order modes. The spectrum was collected in the parallel configuration (HH configuration) with a 2.34 eV excitation laser energy. Each peak was fitted by a Lorentzian function (orange curves). The intensities were multiplied by 1.33 and 1.66 in the second and third panels, respectively, for better visualization of the peaks. Polarized Raman spectra recorded in (b) parallel and (c) crossed configurations for angles varying from 0° to 180°. The sample was rotated in steps of 10° with respect to the fixed incident and scattered light polarization. The 0° corresponds to the alignment along the *b*-axis. In (b) and (c), the spectra is presented for each 20° rotation. The data are not normalized and share the same scale. Raman intensity map in the (d) parallel and (e) crossed configurations, the Raman map is plotted for each 10° rotation. They are normalized separately and the intensities are shown in a logarithmic color scale for better visualization.

$$+\left(v\cos 2\theta\right)^2-\frac{1}{2}\sin 4\theta\left(wv\cos\phi_{wv}-uv\cos\phi_{uv}\right), \tag{4}$$

$$I_{HH+VH}\propto u^2\cos^2\theta+v^2+w^2\sin^2\theta \\ -2v\left(u\cos\phi_{uv}+w\cos\phi_{wv}\right)\sin\theta\cos\theta. \tag{5}$$

Here, θ is the angle between $\hat{e}_s$ and the x-axis and $\phi_{ij}=\phi_i-\phi_j\ (i,j=u,v,w)$ is the phase difference. For a Raman tensor with no relative phases, the equations above are changed by replacing these phase-difference cosines by the unity with $u,v,w\in\mathbb{R}$ (see Supporting Information for details).

2.3. Angular dependence of the Raman intensity

We first attempt to fit the angular dependence of the Raman intensity of each mode shown in figure 1 by considering only real ($\mathbb{R}$) elements for the Raman tensor as discussed above. We also consider the sum of configurations ($I_{HH+VH}=I_{HH}+I_{VH}$) so as to compare our results with previous reports [14, 27]

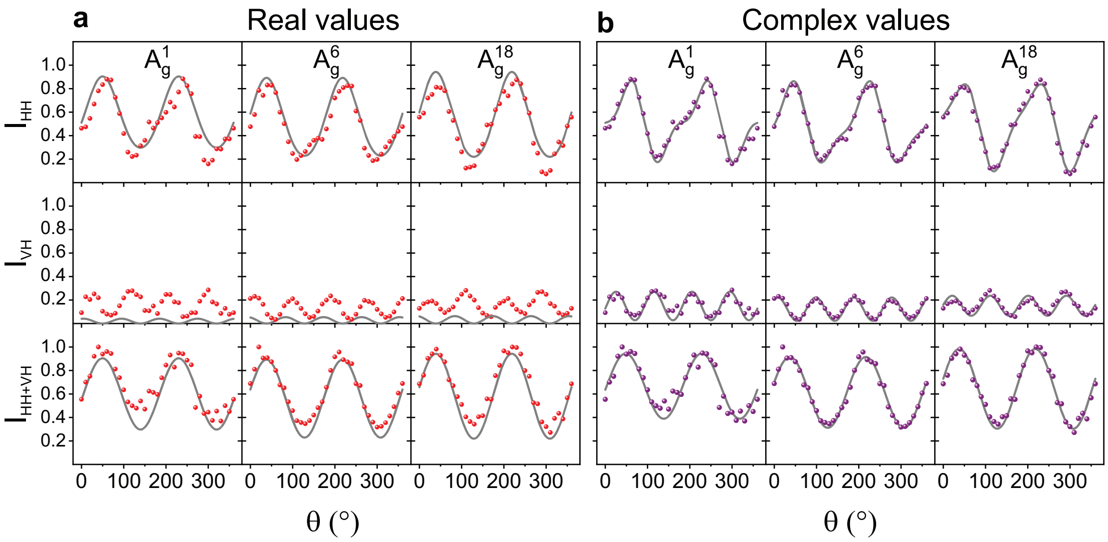

Figure 2. Comparison of the angular dependence of the Raman tensor elements with real and complex values. Angular dependence of the A_g^1 (107.9 cm^{-1}), A_g^6 (175.7 cm^{-1}) and A_g^{18} (297.1 cm^{-1}) modes in single-layer ReSe$_2$, fitted according to equation (1), for Raman tensor with (a) real elements and (b) complex elements. The dots correspond to the experimental data values while solid lines correspond to the fitting. The first, second and third rows correspond to the I_{HH}, I_{VH} and I_{HH+VH}, respectively.

based on experiments in which the scattered light does not pass through an analyzer or polarizer, leading to a scattered intensity represented by the sum of I_{HH} and I_{VH}.

The fitting process of the I_{HH} and I_{VH} as a function of the angle θ as well as their sum was performed simultaneously with shared Raman tensor elements to allow us to unambiguously obtain their modulus and phase differences. In this first attempt, good fits were achieved only for the A_g^7 (178.9 cm^{-1}), A_g^{13} (233.4 cm^{-1}), A_g^{14} (242.5 cm^{-1}), A_g^{15} (251.1 cm^{-1}), and A_g^{16} (264.3 cm^{-1}) modes of a single-layer ReSe$_2$ (see figure S4). However, real number elements do not properly fit the remaining data set. For example, A_g^1 (107.9 cm^{-1}), A_g^6 (175.7 cm^{-1}), and A_g^{18} (297.1 cm^{-1}) modes shown in figure 2 (see figure S5 for other modes). Similar results were obtained for other 2D materials such as black phosphorus [9], WTe$_2$ [11] and MoTe$_2$ [12].

Figure 2(a) shows the fitting of I_{HH}, I_{VH} and I_{HH+VH} versus θ considering only real values for the tensor elements. Notice that, although the polarization data for the parallel and crossed configurations cannot be individually fitted, the sum (I_{HH+VH}) can be reasonably fitted considering only real numbers (see third row in figure 2). This result shows that polarized Raman measurements performed with an unpolarized detection are not suitable for the purpose of finding the Raman tensor elements, and can provide misleading results. Therefore, experiments in both parallel and crossed configurations are needed to correctly determine the tensor elements in these low symmetry systems.

Figure 2(b) shows the fitting of the polarized Raman intensity of the A_g^1 (107.9 cm^{-1}), A_g^6 (175.7 cm^{-1}), and A_g^{18} (297.1 cm^{-1}) modes, but now considering complex ($\mathbb{C}$) numbers in the fitting process for the Raman tensor elements (see equations (3)). From our results, we concluded that Raman tensors with complex numbers are needed to fit the angular dependence of the Raman modes of single-layer ReSe$_2$, with the exception of five modes, for which we found real values: A_g^7 (178.9 cm^{-1}), A_g^{13} (233.4 cm^{-1}), A_g^{14} (242.5 cm^{-1}), A_g^{15} (251.1 cm^{-1}), and A_g^{16} (264.3 cm^{-1}) modes (see figure S4).

Figure 3 shows the angular dependence of the Raman intensities of all the 18 Raman modes of single layer ReSe$_2$ in parallel and crossed configurations as well as for their sum. It can be observed that the direction of the highest intensity for one mode in the parallel configuration is usually not parallel to a crystallographic axis. For the A_g^7 (178.9 cm^{-1}) mode, for example, the Raman tensor is actually diagonal with almost equal components ($R_{xx} \approx R_{yy}$) for a cartesian system in such direction. Although the A_g^5 (161.7 cm^{-1}), A_g^7 (178.9 cm^{-1}), and A_g^8 (181.9 cm^{-1}) modes in figure 3 seem to behave similarly to B_g modes in orthorhombic crystals in terms of their angle-dependent Raman response, since this dependence changes in polarized experiments using other laser lines [20, 22]. The values of the Raman tensor elements given in equations (3)(a) and (b) that fit the angular dependence of all 18 modes are shown in figures 4(a) and (b). Since the intensities are given in arbitrary units, we have only to consider the ratio w/u and v/u. Notice that we cannot observe any trends for

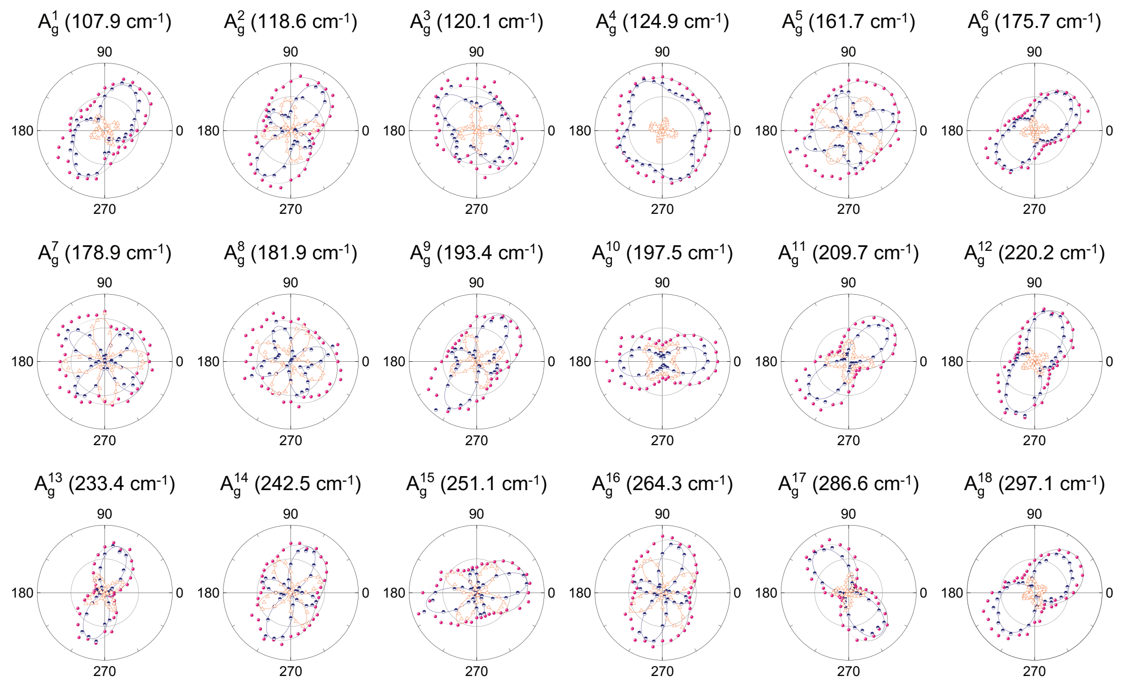

Figure 3. Polar plot of the 18 Raman modes. Angular dependence of the 18 A_g modes in single-layer $ReSe_2$. Blue (orange, pink) symbols correspond to the experimental data of HH (VH, HH+VH) while blue (orange, pink) solid lines correspond to the fit for the same configuration. The gray circles represent half of the total intensity in the polar plots' scale.

the ratio values of the tensor elements for the different modes. This is indeed a consequence of the low symmetry of triclinic $ReSe_2$.

It is important to emphasize that, for crystals with monoclinic (in the case of the *ab*-plane) or higher symmetry, the principal axes of the Raman tensor are necessarily parallel to the crystallographic axes (x, y), and the maxima and minima intensities occur when the light is polarized along these axes. However, this restriction does not occur in triclinic crystals (or monoclinic in the *ac*,*bc*-planes), where the principal axes of the Raman tensor (x', y') do not necessarily coincide with the crystallographic axes (x, y). Figure 4(c) shows the angular dependence of the A_g^{17} (286.6 cm^{-1}) mode, where we can observe the crystallographic coordinate system (x, y) and principal axes (x', y') for this mode, where α is the angle between these two systems. We have performed a similar analysis for all 18 modes, and figure 4(d) shows the obtained values of α for each mode.

We can write all 18 Raman tensor in the coordinate axes (x', y'), where the x'-axis lies on the direction of the maximum intensity in the parallel configuration, which is unique to each mode in $ReSe_2$. Figures 4(e) and (f) show, respectively, the phase differences (ϕ_{uw} and ϕ_{uv}) and the ratio (w/u and v/u) in the new coordinate system for each mode.

Interestingly, the phase differences ϕ_{uw} and ϕ_{uv} in the new coordinate system show a clear trend: the values of the phase difference ϕ_{uw} between the diagonal elements are around $\pi/2$ and π, and the phase difference ϕ_{uv} between the first element of the diagonal and the off-diagonal element is $\pi/2$ (see figure 4(e)). In figure 4(f), one can observe that the Raman tensors with only real elements are diagonal ($v/u = 0$, i.e. all the element exhibit the same phase), contrarily to the case of the Raman tensors with complex elements. Therefore, in this new coordinate system, we can observe that the 18 Raman modes of the single-layer $ReSe_2$ can be grouped according to the values of the Raman tensor elements: (i) diagonal elements, which includes the A_g^7, A_g^{13}, A_g^{14}, A_g^{15} and A_g^{16} modes; (ii) $\phi_{uw}\approx\pi$ and $\phi_{uv} = \pi/2$ phases, consisting of the A_g^2, A_g^5, A_g^8, A_g^{10} and A_g^{11} modes, and (iii) $\phi_{uw}\approx\pi/2$ and $\phi_{uv} = \pi/2$ phase, including the A_g^1, A_g^3, A_g^4, A_g^6, A_g^9, A_g^{12}, A_g^{17} and A_g^{18} modes. Notice that this analysis is valid for the 2.34 eV laser energy, since the polarized Raman response can change when collected using different laser energies (see discussion below). It is noteworthy to mention that no specific trend for w/u and u/v ratios can be discerned even in the new coordinate system despite the fact that its discrepancies are now wiped out. To explain these results, we need to further understand the physical origin of the Raman tensor elements near resonances, within the quantum formalism for the Raman response.

3. Discussion

The results above show that the angular dependence of the polarized Raman spectra of single-layer $ReSe_2$ can only be described considering the complex nature of the Raman tensor elements, in agreement

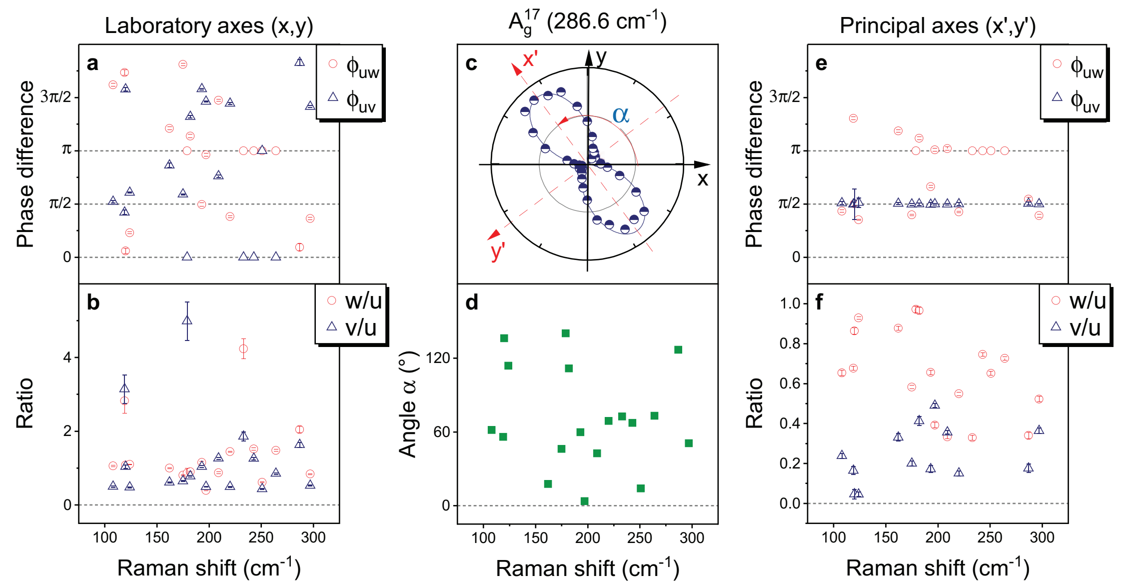

Figure 4. Analysis of the Raman tensor elements. (a) Phase difference between the Raman tensor elements with respect to the laboratory axes. (b) Ratio of the Raman tensor elements and the first diagonal element in the laboratory axes. (c) Scheme of the coordinate system (x', y') using the A_g^{17} (286.6 cm^{-1}) mode as an example. (d) Angle α between the x-axis of the cartesian system for (a) and (b) and the b-axis of the ReSe$_2$ crystal. (e) Phase difference between the Raman tensor elements with respect to the principal axes. (f) Ratio of the Raman tensor elements and the first diagonal element in the principal axes.

with previous observations in other low-symmetry 2D systems [9–12, 19–22]. It is well-known that, for bulk crystals, the birefringence can introduce a relative phase between the Raman tensor elements [23], but this effect can be completely neglected in the case of a single layer material because its thickness is smaller than the wavelength of the incident light. The origin of the complex nature of the Raman tensor elements in a single layer material involves the interactions between photons, electrons and phonons involved in the Raman scattering process.

We will analyse our results considering the quantum formalism of the Raman process, in which the electron–phonon interaction is explicitly taken into account. Within this formalism, the dependence of the component R_{ij}^k of the Raman tensor associated with the k-th mode on the excitation laser energy E_L is given by [36]:

$$R_{ij}^k(E_L) = \frac{1}{V}\sum_{v,c,c'}\sum_{\vec{q}} \frac{\langle\psi_v(\vec{q})|\vec{P}_s\cdot\vec{\nabla}|\psi_{c'}(\vec{q})\rangle\langle\psi_{c'}(\vec{q})|H_{ep}^k|\psi_c(\vec{q})\rangle\langle\psi_c(\vec{q})|\vec{P}_i\cdot\vec{\nabla}|\psi_v(\vec{q})\rangle}{(E_L - E_{cv}(\vec{q}) - i\Gamma_c)(E_L - \hbar\omega_{ph}^k - E_{c'v}(\vec{q}) - i\Gamma_{c'})}, \qquad (6)$$

where V is the crystal volume. We stress that there are other five scattering processes, but we will only consider the fully resonant case involving excited electrons. Further theoretical calculation is needed to specify the contribution of each term in the scattering process. In equation (6), the sum is over the electronic branches ψ_v (in the valence band), ψ_c and $\psi_{c'}$ (in the conduction band) and over all wavevectors $\vec{q}$ within the first Brillouin zone. We only need to consider the states $|\psi_v(\vec{q})\rangle$, $|\psi_c(\vec{q})\rangle$ and $|\psi_{c'}(\vec{q})\rangle$ with the same wavevector $\vec{q}$ since the optical transitions are vertical. In the denominator, $E_{cv}(\vec{q}) = E_c(\vec{q}) - E_v(\vec{q})$ and $E_{c'v}(\vec{q}) = E_{c'}(\vec{q}) - E_v(\vec{q})$ are the energy differences between the valence and conduction bands at a given wavevector $\vec{q}$, and Γ_c and $\Gamma_{c'}$ are the broadening factors associated with the lifetime of photo-excited states $|\psi_c(\vec{q})\rangle$ and $|\psi_{c'}(\vec{q})\rangle$, respectively. The numerator shows the product of three matrix elements: the electron-phonon matrix element $\langle\psi_{c'}(\vec{q})|H_{ep}^k|\psi_c(\vec{q})\rangle$ and two electron-photon matrix elements, $\langle\psi_v(\vec{q})|\vec{P}_s\cdot\vec{\nabla}|\psi_{c'}(\vec{q})\rangle$ and $\langle\psi_c(\vec{q})|\vec{P}_i\cdot\vec{\nabla}|\psi_v(\vec{q})\rangle$, where $\vec{P}_i$ and $\vec{P}_s$ are the polarization vectors of the incident and scattered photons, respectively, along the directions $\hat{e}_i$ and $\hat{e}_s$ introduced in equation (1).

We now discuss the complex nature of the Raman tensor in the scope of the quantum formalism (from equation (6)). Since the electronic functions in non-magnetic crystals can be arranged to be real by taking suitable linear combinations of the Bloch functions with opposite wavevectors, the considered matrix elements are real numbers. Therefore, the origin of the complex nature of R_{ij}^{k} comes from the denominator of equation (6), related to the damping factors Γ_c and $\Gamma_{c'}$.

Let us start considering a particular situation in which only one electronic branch in the valence band (ψ_v) and one electronic branch in the conduction band (ψ_c) are involved in the Raman process ($c = c'$) and that the optical transition occurs in only one specific point $\vec{q}$ within the Brillouin zone. In this very particular case, where we ignored the two sums in equation (6), we can obtain the expression of the phase factor $\phi^k(\vec{q})$ of mode k from the real and imaginary parts of the Raman tensor elements R_{ij}^{k} that is given by:

$$\begin{aligned}\phi^k(\vec{q}) &= \arctan\frac{\mathrm{Im}[R_{ij}^{k}(\vec{q})]}{\mathrm{Re}[R_{ij}^{k}(\vec{q})]}\\ &= \frac{\Gamma_c(2(E_L - E_{cv}(\vec{q})) - \hbar\omega_{ph}^{k})}{(E_L - E_{cv}(\vec{q}))(E_L - E_{cv}(\vec{q}) - \hbar\omega_{ph}^{k}) - \Gamma_c^2}.\end{aligned} \tag{7}$$

Notice from equation (7) that the phase $\phi^k(\vec{q})$ of the Raman tensor, even in the simplest situation where we neglected the two sums in equation (6), depends on different parameters such as the excitation laser energy E_L, the energy gap $E_L - E_{cv}(\vec{q})$, the damping constant Γ_c and the phonon frequency ω_{ph}^{k}.

Let us now consider the sum in equation (6) over all wavevectors $\vec{q}$ within the first Brillouin zone. In this case, the contribution of a specific process with wavevector $\vec{q}$ for the Raman tensor element will be inversely proportional to the difference $E_L - E_{cv}(\vec{q})$. However, we also need to consider the contribution of the numerator of equation (6), that is, the wavevector $\vec{q}$ dependence of the three matrix elements. For the two optical transitions, we also need to take into account the dependence on the polarization directions $\hat{e}_i$ and $\hat{e}_s$. Previous theoretical works have calculated the polarization dependence of these two matrix elements within the dipole approximation, and the results show a two-lobe shaped contribution for each one [10, 37]. The fact that the Raman tensor is different for each mode is a clear evidence that the dependence of the electron-phonon matrix elements on $\vec{q}$ plays a fundamental role to understand the polarization dependencies of the Raman spectra.

In order to highlight the contributions of the electron–phonon interactions for the angular dependence of the Raman results, let us analyse the A_g^9 (193.4 cm^{-1}) and A_g^{10} (197.5 cm^{-1}) modes shown in figure 3. If their electron–phonon interactions were similar, they would also exhibit the same electron–photon coupling, resulting in the same pattern of the angular dependence of the Raman response. However, they exhibit quite a different behavior, and their maxima intensities occur at 60° and 4°, respectively. Thus, our experimental results show how important is the role of the electron–phonon interactions to determine the angular dependence of the Raman spectra in single-layer anisotropic 2D materials.

The above reasoning relies on the anisotropy of electron–phonon interactions, which shows up as a rich phenomenology in the angular dependence of the Raman spectra in single-layer ReSe$_2$. To further verify that such anisotropy is indeed an important feature in our system, we have performed calculations of the electron-phonon coupling within the EPW (Electro-Phonon coupling using Wannier functions)[38]. This scheme applies density-functional perturbation theory (DFPT) combined with localized Wannier functions and a generalized Fourier interpolation to achieve dense Brillouin zone grids. The potential changes due to the phonon modes are perturbatively determined, and the corresponding matrix elements can be calculated for particular choices of electronic states. In turn, the normal modes are given by a previous calculation based on the Quantum Espresso package implementation [39, 40]. Figure 5 shows typical examples of our results. Each plot corresponds to a map of the electron–phonon coupling as a function of the phonon wavevector $\vec{q}$ over the entire Brillouin zone for a chosen normal mode. In figures 5(a) and (b), we chose the aforementioned A_g^9 and A_g^{10} modes, and we considered matrix elements at the **M** point between the same electronic states (the lowest conduction band). Figures 5(c)–(f) show patterns for A_g^4, A_g^5, A_g^9 and A_g^{10}, respectively, calculated at the $\mathbf{\Gamma}$ point, with electronic states limited to the third lowest conduction band. The overall feature, clearly seen in figure 5, is the strong dependence on both the direction of the $\vec{q}$ vector and the choice of the normal mode, reflecting the anisotropic character of the material. Despite the fact that only $\vec{q} \sim 0$ phonons are involved in first-order Raman scattering, the vertical optical transitions occur for all electronic wavevectors $\vec{k}$ within the Brillouin zone. Therefore, the anisotropy of the electron–phonon interactions has an important role not only in transport phenomena but also in Raman measurements. This result is not restricted to diagonal matrix elements. Indeed, we found basically the same features when distinct electronic states are taken into account in the calculation. For instance, we also present the electron-phonon coupling maps for A_g^9 and A_g^{10} modes involving the first and second conduction bands at the **M** point (see figure S6).

Our conclusions can also be extended to explain some results on previous Raman studies of ReSe$_2$ [20, 22]. From the investigation of low-frequency modes, Lorchat *et al* observed that the splitting of the shear modes in bilayers ReSe$_2$, denoted as S^+ and S^- in reference [20], present distinct direction and polarization patterns. The shear modes

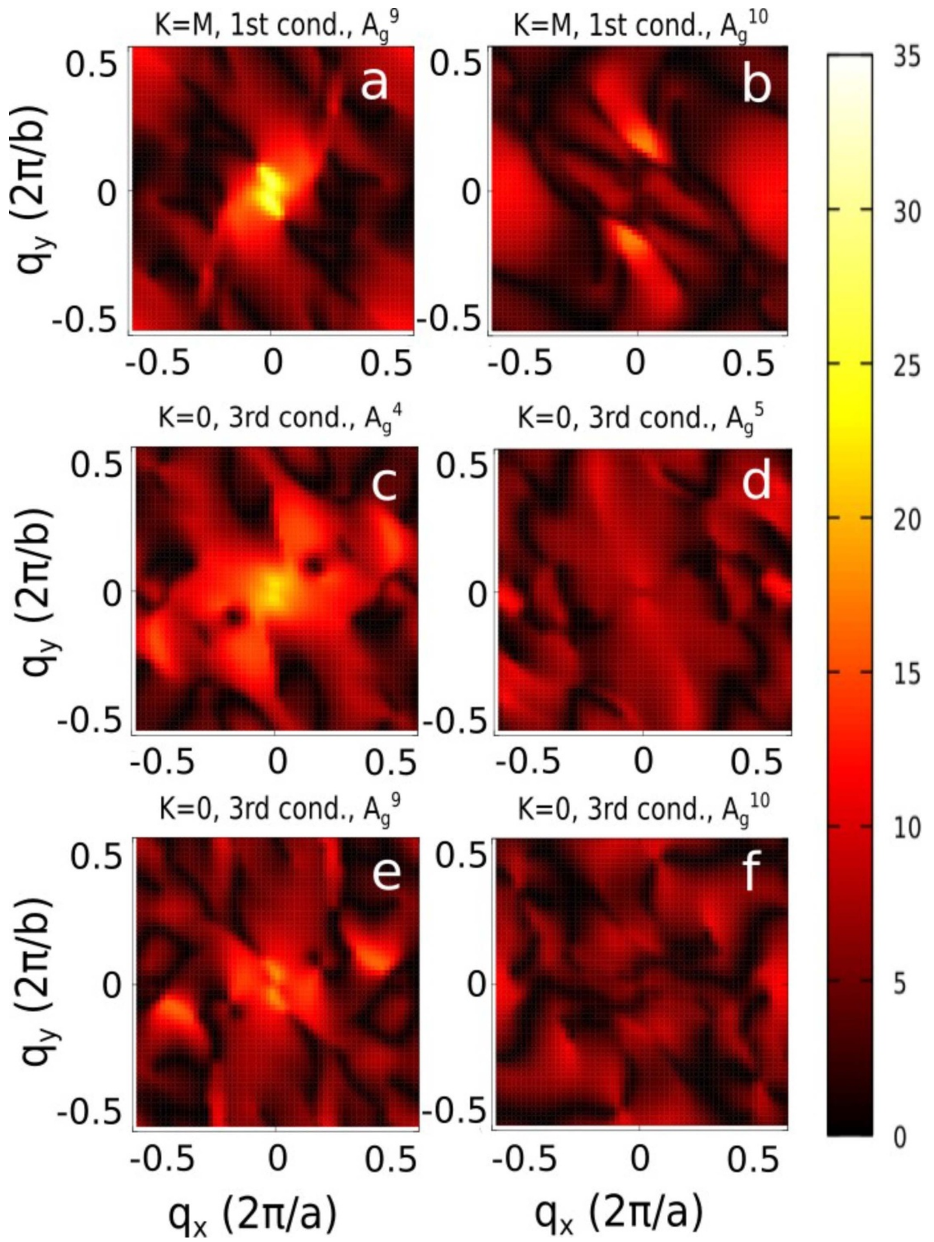

Figure 5. Electron–phonon coupling maps. Calculated electron–phonon couplings for (a) A_g^9 and (b) A_g^{10} between the lowest conduction band electronic states at the **M** point and for (c)–(f) A_g^4, A_g^5, A_g^9, A_g^{10} between the third lowest conduction band electronic stated at the **Γ** point. The colorbar scale is in units of meV.

are about 1 cm^{-1} apart, thus from our conclusions the observed differences of these modes can only be explained considering their unique electron–phonon interactions. In addition, reference [20] also reported a strong dependence of the angular Raman intensity patterns for the 1.96 and 2.33 eV excitation energies, attributed to a possible symmetry-dependent resonant exciton–phonon interaction. In fact, as shown in equation (7), the phase of each mode depends on the excitation laser energy. In the case of low-symmetry materials, this effect completely changes the results for the angular-dependence of the polarized spectra, when they are obtained using different excitation laser lines. Choi *et al* have extended this observed dependence for an excitation energy of 2.81 eV [22]. According to our analysis, the different contributions for the phase in low-symmetry 2D systems not only depend on the excitation energy but also on the lifetime of the excited states, leading to distinct electron-photon polarization dependencies and also to distinct electron-phonon anisotropies.

4. Conclusion

We studied a single layer of ReSe$_2$, a 2D material with the lowest symmetry (triclinic), by angle-resolved polarized Raman spectroscopy, controlling both the incident and scattered light polarization, and using the 2.34 eV excitation laser line. We showed that it is essential to measure the parallel and crossed-polarized spectra to correctly obtain the Raman tensor elements from the analysis of the angle-resolved measurements. We probed all the predicted 18 A_g vibrational modes and determined the Raman tensor elements for all of them from the fitting of the angle-resolved data. We observed that from the tensor elements 13 out of the 18 A_g modes exhibit relative phases, or complex values in the fitting parameters, a result that can be only observed in low symmetry crystals. We showed that it is possible to group the Raman modes in three different classes according to their Raman tensor values, when they are represented in the principal axes coordinate system. The analysis of the Raman tensor elements within the quantum description showed that the phase in low-symmetry 2D systems have different contributions, such as the electronic transitions, the excitation laser energy, the phonon frequency and the lifetime of the excited state. In order to understand the different behavior of the Raman tensor for the 18 modes, we showed that the dependence of the electron-phonon matrix elements on the wavevector $\vec{q}$ play a crucial role. First-principle calculations of the electron-phonon coupling within the DFPT formalism, combined with a Wannier interpolation scheme, show that, indeed, for different phonon modes and wavevector $\overrightarrow{k}$, the maxima for the electron-phonon coupling occur at different points $\vec{q}$ within the Brillouin zone, reflecting the anisotropic character of the 2D triclinic single-layer $ReSe_2$. This result explains why two Raman peaks with very close frequencies can exhibit very different behavior in the angle-resolved measurements. The understanding of the physics underlying the anisotropic properties of the electron–phonon interactions in a 2D material with lowest 2D symmetry can be useful to understand the efficiency of devices affected by electron–phonon interactions, especially for optoelectronic applications using the anisotropic properties of crystals.

5. Methods

5.1. Experimental methods

The single-layer samples were obtained by mechanical exfoliation of a $ReSe_2$ crystals synthesized through chemical vapor transport [18]. Then, the exfoliated flakes were deposited onto a Si substrate with a 300 nm thick SiO_2 coating and a coverslip (glass substrate). The micro-Raman measurements were performed in a HORIBA *Jobin Yvon* triple-monochromator spectrometer equipped with N_2-cooled charge-couple device detectors and with a 1800 g mm^{-1} diffraction grating, giving spectral resolution better than 1 cm^{-1}. The samples were excited by an Ar/Kr ion laser with excitation energy of 2.34 eV (530.8 nm). For the polarized Raman experiments, the samples were placed on a rotating stage and a half-wave plate was placed before the samples to rotate the polarization of the incident light by 90° with an analyzer placed before the spectrometer entry in all measurements. All the measurements were conducted in the backscattering geometry under room-temperature conditions. The samples were focused by a 100× objective (NA = 0.9) providing a spot size of about 2 μm in diameter. The laser power at the sample surface was kept below 0.7 mW in order to avoid sample heating.

5.2. Theoretical methods

To calculate the electron-phonon matrix elements we employed the EPW [38] formalism via a Wannier interpolation scheme. First, we carried out DFT and DFPT calculations, as implemented in the QUANTUM ESPRESSO distribution [39, 40]. The exchange-correlation energy was treated using PBE scalar-relativistic norm-conserving pseudopotentials [41]. Electronic wave functions are expanded in a plane-wave basis with kinetic energy cutoffs of 85 *Ry*. The initial unit cell for single-layer $ReSe_2$ was constructed by using atomic positions obtained by x-ray diffraction experiments [25]. Then, the positions and lattice vectors were relaxed until the convergence criteria for the total energy and total forces minimization were smaller than 1.0×10^{-4} *Ry* and 1.0×10^{-3} *Ry*/*Bohr*, respectively. To perform the EPW calculations, we used a coarse $12 \times 12 \times 1$ k-mesh and a $4 \times 4 \times 1$ $\vec{q}$-point grid for electrons and phonon integration, respectively. Then, we generated electron-phonon maps along the Brillouin zone by fixing a **k**-point, selecting two conduction band indexes, a phonon branch, and then sampling the $\vec{q}$-space considering a finer uniform $60 \times 60 \times 1$ grid.

Data availability

All relevant data are available from the authors upon request.

Acknowledgments

We thank Roberto L. Moreira and Eliel G. S. Neto for helpful discussions. G C R, G A S R, J S L, J C B, M S C M, C F, B R C and M A P acknowledge the financial support from the Brazilian agencies CNPq, CAPES, FAPEMIG, and Brazilian Institute of Science and Technology in Carbon Nanomaterials (INCT-Nanocarbono). M S C M, G A S R and O J S acknowledge the Aalto Science-IT project and CSC, Helsinki for the computational resources. L B acknowledges support from the US National Science Foundation through DMR grant # 1807969. M T thanks the Air Force Office of Scientific Research (AFOSR) Grant No. FA9550-18-0072.

Author contributions

G C R, B R C and M A P conceived the idea and designed the experiments; G C R and C F performed the polarized Raman experiments; G C R analysed and interpreted the experimental data; G A S R, O

J S and M S C M performed the electron-phonon matrix elements calculation and theoretical analysis; J S L and J C B prepared the single-layer flakes and performed optical microscopy; D R, L B and M T provided the $ReSe_2$ crystals; G C R, B R C and M A P wrote the manuscript. The work was supervised by B R C and M A P; All the authors discussed the results and commented on the manuscript.

Additional information

Supporting Information is available from the website or from the author.

Competing interests

The authors declare that they have no competing interests.

ORCID iDs

Geovani C Resende https://orcid.org/0000-0003-4419-9448
Jessica S Lemos https://orcid.org/0000-0002-9493-9240
Juliana C Brant https://orcid.org/0000-0002-8931-3403
Luis Balicas https://orcid.org/0000-0002-5209-0293
Mauricio Terrones https://orcid.org/0000-0003-0010-2851
Mario S C Mazzoni https://orcid.org/0000-0001-5897-6936
Cristiano Fantini https://orcid.org/0000-0003-0436-7857
Bruno R Carvalho https://orcid.org/0000-0001-5188-8685
Marcos A Pimenta https://orcid.org/0000-0002-3389-0682

References

[1] Novoselov K S, Geim A K, Morozov S V, Jiang D, Zhang Y, Dubonos S V, Grigorieva I V and Firsov A A 2004 *Science* **306** 666–9
[2] Novoselov K S, Jiang D, Schedin F, Booth T J, Khotkevich V V, Morozov S V and Geim A K 2005 *Proc. Natl. Acad. Sci. U.S.A.* **102** 10451–3
[3] Mounet N *et al* 2018 *Nat. Nanotechnol.* **13** 246
[4] Fei R and Yang L 2014 *Nano Lett.* **14** 2884–9
[5] Qiao J, Kong X, Hu Z-X, Yang F and Ji W 2014 *Nat. Commun.* **5** 4475
[6] Tao J *et al* 2015 *ACS Nano* **9** 11362–70
[7] Luo Z, Maassen J, Deng Y, Du Y, Garrelts R P, Lundstrom M S, Ye P D and Xu X 2015 *Nat. Commun.* **6** 8572
[8] Wang X *et al* 2015 *Nat. Nanotechnol.* **10** 517
[9] Ribeiro H B, Pimenta M A, de Matos C J S, Moreira R L, Rodin A S, Zapata J D, de Souza E A T and Castro Neto A H 2015 *ACS Nano* **9** 4270–6
[10] Ling X *et al* 2016 *Nano Lett.* **16** 2260–7
[11] Song Q *et al* 2016 *Sci. Rep.* **6** 29254
[12] Beams R *et al* 2016 *ACS Nano* **10** 9626–36
[13] Chenet D A, Aslan O B, Huang P Y, Fan C, van der Zande A M, Heinz T F and Hone J C 2015 *Nano Lett.* **15** 5667–72
[14] Wolverson D, Crampin S, Kazemi A S, Ilie A and Bending S J 2014 *ACS Nano* **8** 11154–64
[15] Yang S *et al* 2015 *Nano Lett.* **15** 1660–6
[16] Zhang E *et al* 2016 *ACS Nano* **10** 8067–77
[17] Yang S, Tongay S, Li Y, Yue Q, Xia J, Li S, Li J and Wei S 2014 *Nanoscale* **6** 7226–31
[18] Pradhan N R *et al* 2018 *Sci. Rep.* **8** 12745
[19] Strach T, Brunen J, Lederle B, Zegenhagen J and Cardona M 1998 *Phys. Rev.* B **57** 1292–7
[20] Lorchat E, Froehlicher G and Berciaud S 2016 *ACS Nano* **10** 2752–60
[21] Phaneuf-L'Heureux A-L, Favron A, Germain J-F, Lavoie P, Desjardins P, Leonelli R, Martel R and Francoeur S 2016 *Nano Lett.* **16** 7761–7
[22] Choi Y, Kim K, Lim S Y, Kim J, Park J M, Kim J H, Lee Z and Cheong H 2020 *Nanoscale Horiz.* **5** 308–15
[23] Kranert C, Sturm C, Schmidt-Grund R and Grundmann M 2016 *Phys. Rev. Lett.* **116** 127401
[24] Wilson J A and Yoffe A D 1969 *Adv. Phys.* **18** 193–335
[25] Lamfers H-J, Meetsma A, Wiegers G A and de Boer J L 1996 *J. Alloys Compd.* **241** 34–9
[26] Jariwala B, Thamizhavel A and Bhattacharya A 2017 *J. Phys. D Appl. Phys.* **50** 044001
[27] Zhao H, Wu J, Zhong H, Guo Q, Wang X, Xia F, Yang L, Tan P and Wang H 2015 *Nano Res.* **8** 3651–61
[28] Hart L, Dale S, Hoye S, Webb J L and Wolverson D 2016 *Nano Lett.* **16** 1381–6
[29] Taube A, Łapińska A, Judek J and Zdrojek M 2015 *Appl. Phys. Lett.* **107** 013105
[30] Liu C, Ma Y, Li W and Dai L 2013 *Appl. Phys. Lett.* **103** 213103
[31] Zhang H, Wan Y, Ma Y, Wang W, Wang Y and Dai L 2015 *Appl. Phys. Lett.* **107** 101904
[32] Carvalho B R, Malard L M, Alves J M, Fantini C and Pimenta M A 2015 *Phys. Rev. Lett.* **114** 136403
[33] Wang H, Liu E, Wang Y, Wan B, Ho C-H, Miao F and Wan X G 2017 *Phys. Rev.* B **96** 165418
[34] McCreary A *et al* 2017 *Nano Lett.* **17** 5897–907
[35] Yu P Y and Cardona M 2010 *Fundamentals of Semiconductors* Fourth ed. (London New York: Springer, Heidelberg Dordrecht)
[36] Loudon R 1964 *Adv. Phys.* **13** 423–82
[37] Huang S *et al* 2016 *ACS Nano* **10** 8964–72
[38] Noffsinger J, Giustino F, Malone B D, Park C-H, Louie S G and Cohen M L 2010 *Comput. Phys. Commun.* **181** 2140–8
[39] Giannozzi P *et al* 2009 *J. Phys. Condens. Matter* **21** 395502
[40] Giannozzi P *et al* 2017 *J. Phys. Condens. Matter* **29** 465901
[41] van Setten M J, Giantomassi M, Bousquet E, Verstraete M J, Hamann D R, Gonze X and Rignanese G-M 2018 *Comput. Phys. Commun.* **226** 39–54